Randomness, Symmetry, and Scaling of Mesoscale Eddy Life Cycles

Citation	Samelson, R. M., M. G. Schlax, D. B. Chelton, 2014: Randomness, Symmetry, and Scaling of Mesoscale Eddy Life Cycles. Journal of Physical Oceanography, 44, 1012–1029. doi:10.1175/JPO-D-13-0161.1
DOI	10.1175/JPO-D-13-0161.1
Publisher	American Meteorological Society
Version	Version of Record
Citable Link	http://hdl.handle.net/1957/47889
Terms of Use	http://cdss.library.oregonstate.edu/sa-termsofuse

Randomness, Symmetry, and Scaling of Mesoscale Eddy Life Cycles

R. M. SAMELSON, M. G. SCHLAX, AND D. B. CHELTON

College of Earth, Ocean, and Atmospheric Sciences, Oregon State University, Corvallis, Oregon

(Manuscript received 16 July 2013, in final form 2 December 2013)

ABSTRACT

It is shown that the life cycles of nonlinear mesoscale eddies, a major component of low-frequency ocean physical variability, have a characteristic structure that differs fundamentally from that which would be expected on the basis of classical interpretations of ocean eddy evolution in terms of mean flow instability and equilibration followed by frictional, radiative, or barotropic decay, or of vortex merger dynamics in quasigeostrophic turbulent cascades. Further, it is found that these life cycles can be accurately modeled in terms of the large-amplitude excursions of a stochastic process. These conclusions, which apply in the corresponding global-mean context, follow from the examination of ensemble-mean and standard deviation time series of normalized eddy amplitude from an automated eddy identification and tracking analysis of a nearly two decade–merged satellite altimeter record of global sea surface height (SSH). The resulting series are found to have several striking and unexpected characteristics, including time-reversal symmetry and approximate self-similarity. Consistent results are obtained from a similar analysis of a 7-yr record of global SSH from a numerical ocean circulation model. The basic qualitative and quantitative statistical properties of these series can be remarkably well reproduced with an extremely simple stochastic model, in which the SSH increments between successive time points are random numbers, and the eddy life cycles are represented by excursions exceeding a given threshold. The stochastic model is found also to predict accurately the empirical autocorrelation structure of the underlying observed SSH field itself, when the autocorrelations are computed along long planetary (Rossby) wave characteristics.

1. Introduction

The ocean mesoscale, away from boundary currents, is characterized by energetic variability and fluctuating horizontal currents that are typically at least one order of magnitude faster than the long-term mean (Dantzler 1977; Wyrtki et al. 1976; MODE Group 1978; Wunsch 1981; McWilliams et al. 1983; Robinson 1983; Schmitz et al. 1983). This mesoscale variability has important effects on ocean biology, on the momentum and heat balances of the lower atmosphere, and on the ocean's role in Earth's climate system (Wunsch 1999; Martin and Richards 2001; Henning and Vallis 2005; McGillicuddy et al. 2007, 2008; Wolfe et al. 2008; Wolfe and Cessi 2010; Anderson et al. 2011; Chelton et al. 2011a; Gaube 2012; Gaube et al. 2014). Interpretations of its dynamical character have ranged from linear wave theory (Müller and Frankignoul 1981; Killworth et al. 1997) to geostrophic turbulence (Rhines 1975, 1977, 1979; Salmon 1980; Smith and Vallis 2002). Several decades of focused attention have yielded many significant advances including synoptic, in situ measurements of energetic, baroclinic, eddy three-dimensional structure and evolution (MODE Group 1978) broadly consistent with β-plane wave turbulence theory (Rhines 1975, 1977). However, global observations of systematic westward propagation (Chelton and Schlax 1996; Fu 2009; Chelton et al. 2011b) in suggestive accord with general expectations for both linear (Gill 1982; Pedlosky 1987) and isolated nonlinear (McWilliams and Flierl 1979) features, and numerous fundamental insights from a wide variety of theoretical, laboratory, and numerical modeling studies (e.g., Bretherton 1966; Larichev and Held 1995; Xu and Fu 2011; Smith and Vallis 2002; Tulloch et al. 2009; Venaille et al. 2011), a comprehensive and definitive rationalization of the mesoscale regime has not yet been achieved.

Recently, a new, quantitative, global description of ocean mesoscale variability has become available through the development and application by Chelton et al. (2011b) of an automated eddy identification and tracking procedure to a nearly two-decade global record of merged

Denotes Open Access content.

Corresponding author address: R. M. Samelson, College of Earth, Ocean, and Atmospheric Sciences, 104 CEOAS Admin. Bldg., Oregon State University, Corvallis, OR 97331-5503.
E-mail: rsamelson@coas.oregonstate.edu

DOI: 10.1175/JPO-D-13-0161.1

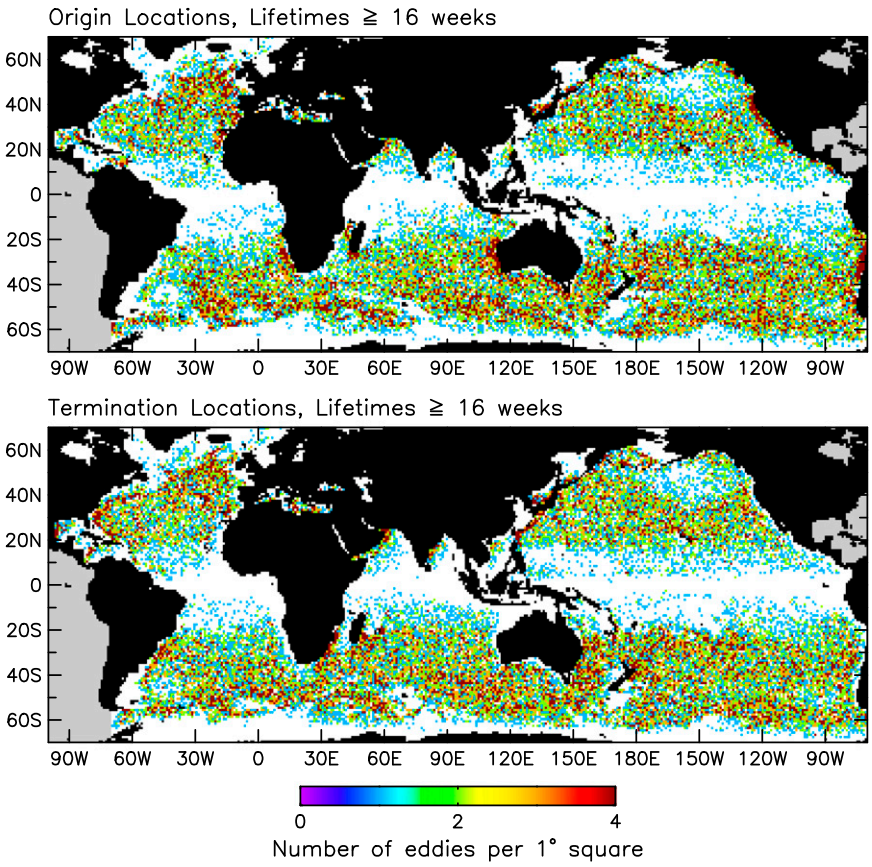

FIG. 1. Census statistics for altimetry-tracked eddies with lifetimes ≥16 weeks, showing the numbers of eddy (top) originations and (bottom) terminations in each $1° \times 1°$ region over the 19.5-yr period from October 1992 through April 2012. Modified from Fig. 6 of Chelton et al. (2011b).

satellite altimeter observations of sea surface height (SSH). This approach uses an amplitude threshold and several other criteria to identify and track coherent, isolated, mesoscale vortex features, which are referred to by Chelton et al. (2011b) as "eddies" and may also be described as nonlinear planetary (Rossby) waves. Their nonlinear character can be inferred from the large observed ratios U/c of their geostrophic current speeds U and propagation speeds c, which almost uniformly satisfy $U/c > 1$, a classical nonlinearity measure in fluid mechanics indicating that fluid may be trapped and transported with the coherent features. Their nonlinearity is evident also from comparisons of observed wavenumber–frequency spectra with linear and nonlinear model spectra, in which the observations consistently show nondispersive propagation at all resolved wavelengths, including the short wavelengths at which linear theory would predict dispersion (Chelton et al. 2011a; Early et al. 2011). The wavelike aspect of their character is evinced by the approximate match between their observed propagation speeds and the theoretical speeds of long planetary waves linearized about a climatological mean ocean state. The origination and termination points of the altimeter-tracked eddies are broadly distributed across the midlatitude oceans (Fig. 1); while concentrations of originations and terminations are detectable near eastern and western boundaries, respectively, these localized intensifications do not dominate the geographical distributions (Chelton et al. 2011b).

The algorithm employed by Chelton et al. (2011b) yields a measure of the amplitude of each identified eddy feature. The time histories of these amplitudes are studied systematically here for the first time, as representations of eddy life cycles. In this initial study, the entire global eddy dataset is considered, and no attempt at geographical differentiation or regionally specific analysis is made. It is shown here that these amplitude-based eddy life cycles have striking and unexpected global-mean statistical characteristics, including time-reversal symmetry and approximate self-similarity. Their structure differs fundamentally from that which would be expected on the basis of classical interpretations of ocean eddy evolution in terms of mean

flow instability and nonlinear equilibration followed by frictional, radiative, or barotropic decay, or of vortex merger dynamics in quasigeostrophic turbulent cascades; a more general consistency with geostrophic turbulence theory is still possible. Further, the basic qualitative and quantitative statistical properties of these series can be remarkably well reproduced with an extremely simple stochastic model, in which the SSH increments between successive time points are random numbers, and the eddy life cycles are represented by excursions exceeding a given threshold. The stochastic model is found also to predict accurately the empirical autocorrelation structure of the underlying observed SSH field itself, when the autocorrelations are computed along long planetary (Rossby) wave characteristics.

2. Altimeter-tracked eddy amplitude time series

a. Eddy dataset

The altimeter-tracked eddy dataset used in this analysis was obtained by applying the eddy identification and tracking procedure described by Chelton et al. (2011b) to the 19.5-year (from October 1992 through April 2012) version of the Archiving, Validation, and Interpretation of Satellite Oceanographic data (AVISO) Reference Series merged satellite SSH anomaly dataset constructed by Segment Sol multimissions d'ALTimétrie, d'Orbitographie et de localisation precise/Data Unification and Altimeter Combination System (SSALTO/DUACS) using the approach summarized by Ducet et al. (2000). While the alternative AVISO Updated Series, based on simultaneous measurements from up to four altimeters, might be expected potentially to resolve smaller-scale eddies, the availability of more than the two altimeters used to construct the AVISO Reference Series is spotty over most of the 19.5-year time period analyzed for this study; moreover, we have concluded from explorations of this alternative dataset that the use of the same spatial correlation functions in the objective analysis procedure for both the Reference and Updated Series results in the two series having no detectable difference in resolution capability.

The eddy identification algorithm (Chelton et al. 2011b) defines an eddy as "a simply connected set of pixels that satisfy the following criteria: (1) The [spatially high-pass filtered or 'anomaly'] SSH values of all of the pixels are above (below) a given SSH threshold for anticyclonic (cyclonic) eddies. (2) There are at least 8 pixels and fewer than 1000 pixels comprising the connected region. (3) There is at least one local maximum (minimum) of SSH for anticyclonic (cyclonic) eddies. (4) The amplitude of the eddy is at least 1 cm. (5) The distance between any pair of points within the connected region must be less than a specified maximum." The SSH threshold was varied systematically between ± 1 m in steps of 1 cm, and all maximal eddy perimeters satisfying the preceding criteria were identified in each weekly global-merged SSH field. The eddy amplitude is computed as the difference between the maximum SSH anomaly in the eddy interior and the mean SSH around the identified maximal eddy perimeter. Eddies with positive and negative SSH anomalies correspond to anticyclones and cyclones, respectively; in both cases, the corresponding amplitudes were taken as positive and a separate index equal to ± 1 distinguished anticyclonic and cyclonic polarities. An automated procedure, based on searches through restricted nearby areas consistent with anticipated regional bounds on eddy propagation speeds, was then applied to identify and trace the trajectory of each eddy from week to week. (The altimeter-tracked eddy dataset used in this analysis is available online at http://cioss.coas.oregonstate.edu/eddies/.) Further details of the method are described by Chelton et al. (2011b).

The altimeter-tracked eddy dataset includes a time series of weekly values of eddy amplitude for each tracked eddy, $\{A_k(t_j): t_j = j\Delta t;\ j = 1, 2, \ldots, J_k;\ k = 1, 2, \ldots, K\}$, where there are a total of K-tracked anticyclonic and cyclonic eddies, $\Delta t = 1$ week, the kth eddy has lifetime $L_k = J_k \Delta t$ weeks, the amplitudes $A_k(t_j)$ are all positive, and the curly brackets denote a collection of objects. For the dataset analyzed here, $K \approx 2 \times 10^5$, and the minimum and maximum lifetimes were 4 and 307 weeks, respectively. Individual eddy amplitude time series show numerous large positive and negative increments on time scales of weeks (Fig. 2a). For some altimeter-tracked eddies (e.g., Fig. 2a), independent RAFOS float data records are available that confirm their coherent Lagrangian character (Collins et al. 2013). The corresponding float pressure and velocity records show large fluctuations on time scales comparable to those of the amplitude fluctuations for the altimeter-tracked eddies in which they are embedded, indicating a general qualitative consistency between the remote sensing (altimeter) and in situ (float) measurements. Definitive, quantitative comparison of the altimeter and float observations is complicated by the essentially different time and space resolutions of the respective datasets. Such a comparison is in progress but is beyond the scope of the present work.

b. Analysis and results

The set of altimeter-tracked eddy amplitudes with lifetimes L between 4 and 156 weeks were studied, with particular focus on the range $16 \le L \le 80$ weeks. Each eddy amplitude time series $\{A_k\}$ was normalized by its time mean $\overline{A}_k = J_k^{-1} \sum_j A_k(t_j)$. The normalized amplitude time series $\{\hat{A}_k: \hat{A}_k(t_j) = A_k(t_j)/\overline{A}_k\}$ were sorted into sets

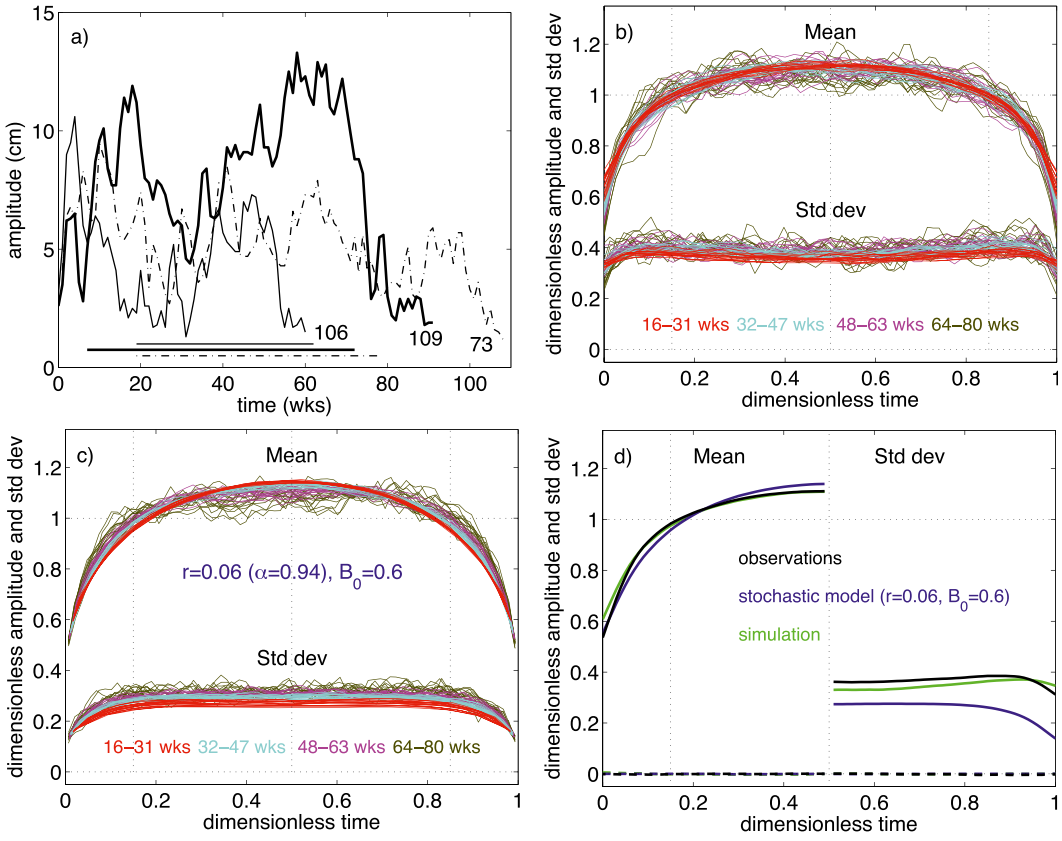

FIG. 2. (a) Three amplitude time series from altimeter-tracked eddies. For these eddies, observations from embedded RAFOS floats [numbers 73, 106, and 109 of Collins et al. (2013)] during the indicated time periods (horizontal lines) confirm their coherent Lagrangian character. (b) Ensemble mean $\mathcal{A}^L$ and std dev $\mathcal{S}^L$ of normalized amplitude vs dimensionless time τ for altimeter-tracked eddies for each lifetime L, $16 \le L \le 80$ weeks. (c) As in (b), but for stochastic model with $r = 0.06$ and $B_0 = 0.6$. (d) Overall mean time-symmetric ($\mathcal{A}_s, \mathcal{S}_s$; black solid) and time-antisymmetric ($\mathcal{A}_a, \mathcal{S}_a$; black dashed) normalized ensemble mean ($\mathcal{A}_s, \mathcal{A}_a$; $0 < \tau < 0.5$) and std dev ($\mathcal{S}_s, \mathcal{S}_a$; $0.5 < \tau < 1$) of normalized amplitude vs dimensionless time τ for all altimeter-tracked eddies with 16–80-week lifetimes, computed from weighted averages of $\mathcal{A}^L$ and $\mathcal{S}^L$. The antisymmetric parts $\mathcal{A}_a$ and $\mathcal{S}_a$ are uniformly small (dashed lines). The corresponding overall mean amplitude and std dev time series are also shown for the stochastic model with $r = 0.06$ and $B_0 = 0.6$ (blue) and for the dynamical simulation (green).

with equal lifetimes, $\{\hat{A}_k\}^L = \{\hat{A}_k : L_k = L\}$; for each lifetime $L = J\Delta t$, $4 \le J \le 156$. The ensemble-mean $\mathcal{A}^L(t_j)$ and standard deviation $\mathcal{S}^L(t_j)$ over each of these sets at each weekly time step t_j were then computed, giving a single pair of mean and standard deviation time series of length J at each lifetime $L = J\Delta t$:

$$\mathcal{A}^L(t_j) = \text{mean}_{\{k:L_k=L\}}\{\hat{A}_k(t_j)\}, j = 1, 2, \ldots, J; \quad \text{and} \tag{2.1}$$

$$\mathcal{S}^L(t_j) = (\text{mean}_{\{k:L_k=L\}}\{[\hat{A}_k(t_j)]^2\} - [\mathcal{A}^L(t_j)]^2)^{1/2}, \quad j = 1, 2, \ldots, J. \tag{2.2}$$

The respective lifetimes L were also each normalized to unity by transforming the weekly time points t_j to a dimensionless time τ according to $\tau_j = (t_j - 1/2)/L$ for each lifetime L. This convention implies that $\tau_1 = 1/(2J)$ and $\tau_L = 1 - 1/(2J)$ and preserves an interpretation of the original time series points as nominal means over 1-week intervals centered on the observation times. An alternative convention would set $\tau_1 = 0$ and $\tau_L = 1$, effectively redefining the dimensional lifetime of each eddy as $L - 1$ week; the two conventions yield essentially identical results. The normalized mean and standard deviation time series were decomposed into time-symmetric and time-antisymmetric parts, according to $\mathcal{A}_s(\tau) = [\mathcal{A}(\tau) + \mathcal{A}(1-\tau)]/2$, $\mathcal{A}_a(\tau) = [\mathcal{A}(\tau) - \mathcal{A}(1-\tau)]/2$, $\mathcal{S}_s(\tau) = [\mathcal{S}(\tau) + \mathcal{S}(1-\tau)]/2$, and $\mathcal{S}_a(\tau) = [\mathcal{S}(\tau) - \mathcal{S}(1-\tau)]/2$, where the subscripts s and a denote time symmetric and time antisymmetric, respectively.

The dimensionless ensemble-mean and standard deviation amplitude time series $\mathcal{A}^L$ and $\mathcal{S}^L$, computed by

(2.1) and (2.2) over equal lifetime classes $\{\hat{A}_k\}^L$ of amplitude time series normalized by their respective time means, have three striking and unexpected characteristics (Fig. 2b). First, they are symmetric to time reversal: the series look essentially identical if the direction of time is reversed. Second, they are approximately self-similar: the mean doubly (amplitude and time) normalized time histories are nearly independent of lifetime L. Third, the ensemble-mean amplitude cycles have a simple, single-hump structure with negative curvature throughout the cycle. The mean-normalized initial and final amplitudes are approximately 0.6, indicating that for each lifetime the mean initial and final amplitudes are slightly greater than half of the mean amplitude over the life cycle. The standard deviations are nearly constant at approximately 0.4, decreasing slightly toward midcycle, with relatively abrupt decreases to 0.3 at the end and beginning of the cycle. The mean amplitude cycles may be divided into intervals of amplitude growth from the initial value to the unit mean value during $0 < \tau \lesssim 0.15$, central intervals of slow growth followed by slow decay during $0.15 \lesssim \tau \lesssim 0.85$, and decay intervals during $0.85 \lesssim \tau < 1$. The approximate self-similarity requires that the lengths of each of these three intervals scale with eddy lifetime, so that the relative proportions remain constant: in the mean, eddies with longer lifetimes have longer initial growth and final decay intervals than eddies with shorter lifetimes.

A single overall mean pair of ensemble-mean and standard deviation life cycles, $\mathcal{A}(\tau)$ and $\mathcal{S}(\tau)$, $0 < \tau < 1$, was computed as weighted means of the corresponding time series $\mathcal{A}^L(\tau)$ and $\mathcal{S}^L(\tau)$ for all lifetimes L with $16 \le L \le 80$ weeks, with weighting proportional to the number of eddies with each lifetime. These normalized mean and standard deviation time series were further decomposed into time-symmetric and time-antisymmetric parts: $\mathcal{A}_s(\tau), \mathcal{A}_a(\tau), \mathcal{S}_s(\tau)$, and $\mathcal{S}_a(\tau)$, where the subscripts s and a denote time symmetric and time antisymmetric, respectively. A total of 41 299 altimeter-tracked eddy amplitude time series had lifetimes L that satisfied the criterion $16 \le L \le 80$ weeks and were included in the calculation of the overall ensemble-mean and standard deviation series, $\mathcal{A}(\tau)$ and $\mathcal{S}(\tau)$. Eddies with lifetimes L satisfying $L < 16$ or $L > 80$ weeks were excluded from this calculation because the physical interpretation of altimeter-tracked eddies as persistent coherent structures was conservatively viewed as potentially unreliable for the shorter lifetimes, while small sample sizes limit statistical reliability for the longer lifetimes. The overall mean series are time-reversal symmetric ($\mathcal{A}_a$ and $\mathcal{S}_a$ are negligible) and capture the approximately self-similar structure of the observed means at each lifetime (Figs. 2b,d).

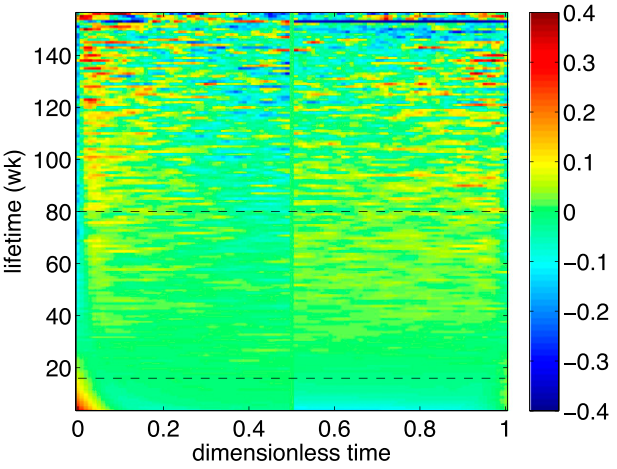

FIG. 3. Differences (shading) $\mathcal{A}_s^L - \mathcal{A}_s, \mathcal{S}_s^L - \mathcal{S}_s$ of time-symmetric lifetime L and overall ensemble mean ($0 < \tau < 0.5$) and std dev ($0.5 < \tau < 1$) of normalized amplitude vs dimensionless time τ, for altimeter-tracked eddies with lifetimes 4–156 weeks. The min (16 weeks) and max (80 weeks) lifetimes for the overall mean (Fig. 2d) are indicated (dashed lines). The antisymmetric differences $\mathcal{A}_a^L - \mathcal{A}_a, \mathcal{S}_a^L - \mathcal{S}_a$ are uniformly small and are not shown.

The mean life cycles at each lifetime L may be similarly decomposed into symmetric and antisymmetric parts, denoted $\mathcal{A}_s^L(\tau), \mathcal{A}_a^L(\tau), \mathcal{S}_s^L(\tau)$, and $\mathcal{S}_a^L(\tau)$. The differences $\mathcal{A}_s^L - \mathcal{A}_s, \mathcal{A}_a^L - \mathcal{A}_a, \mathcal{S}_s^L - \mathcal{S}_s$, and $\mathcal{S}_a^L - \mathcal{S}_a$ of the mean lifetime L series and the corresponding overall 16–80-week mean series at each time point are less than 0.1 almost everywhere for $16 \le L \le 80$ weeks (Fig. 3). For lifetimes $L > 30$ weeks, the difference $\mathcal{A}_s^L - \mathcal{A}_s$ of the mean time-symmetric amplitude series is near -0.1 at $\tau = 0$ (and thus at $\tau = 1$ because of the symmetry), indicating that the initial and final amplitude values for these longer lifetime, mean-normalized time series are measurably smaller than for the overall 16–80-week series mean. There is an indication of a trend in $\mathcal{A}_s^L - \mathcal{A}_s$ toward larger values for $0.02 < \tau < 0.25$ (and thus $0.75 < \tau < 0.98$) and smaller values for $0.25 < \tau < 0.5$ (and thus $0.5 < \tau < 0.75$) with increasing L, which would correspond to a midcycle flattening of the mean amplitude series at longer lifetime. There is a discernible trend in the difference $\overline{\mathcal{S}}_s^L - \mathcal{S}_s$ with increasing L, from near 0 at $L = 16$ weeks to near 0.05 at $L = 80$ weeks, corresponding to a small increase with lifetime of the normalized standard deviations (also visible in Fig. 2b). In contrast, the differences of the time-antisymmetric series are uniformly small and show no evident structure except increasing fluctuations with lifetime L, as the number of eddies contributing to each mean decreases and noise in the estimates increases.

The mean dimensional amplitude $\overline{A}^L$ at each lifetime L, computed as

$$\overline{A}^L = \text{mean}_{\{k:L_k=L\}}\{\overline{A}_k\}, \tag{2.3}$$

increases rapidly with lifetime L for $L < 20$ weeks, becoming progressively less dependent on lifetime with increasing lifetime and nearly independent of lifetime for $L > 40$ weeks (Fig. 4a). This mean amplitude increase with lifetime is qualitatively consistent with previous analysis of the altimeter-tracked eddy dataset (Chelton et al. 2011b, their Fig. 11). The mean dimensional standard deviation $\overline{A}^L\overline{S}^L$ is a nearly constant fraction $\overline{S}^L \approx \overline{S} \approx 0.4$ of the mean amplitude $\overline{A}^L$ (Fig. 4a; see also Figs. 2b and 3). The mean dimensional initial and final amplitudes depend only weakly on L for $L > 16$ weeks, decreasing slightly with lifetime (Fig. 4a). The number distribution of tracked eddies versus lifetime L decays approximately as an inverse-square power law for lifetimes $L \lesssim 40$ weeks and exponentially with the e-folding scale $L_0 = 25$ weeks for $L \gtrsim 40$ weeks (Fig. 4b).

c. *Eddy fluid speed and radius scales*

The altimeter-tracked eddy algorithm yields an estimate of maximum azimuthal geostrophic fluid speed around the eddy and of a horizontal area-equivalent radius scale for each eddy at each time (Chelton et al. 2011b). Statistical analyses analogous to those carried out on the amplitude time series can be carried out for the speed and radius scales, and yield ensemble-mean time series and amplitude and number distributions versus lifetime that qualitatively resemble the results obtained for the amplitude time series (Fig. 5). At zero time lag, over the entire tracked eddy dataset, the correlation of the fluid speed scale with the eddy amplitude is roughly 0.9, while the correlations of the radius scale with the amplitude and the speed scale are both positive and less than 0.2. Thus, the amplitude and speed scales contain similar information, with the speed fluctuations primarily reflecting a geostrophic response to fluctuations in amplitude at fixed eddy radius scale, while the radius scale fluctuates essentially independently, but with relatively weak dependence of the mean radius scale on lifetime. Consequently, analysis of the speed and radius scales appears to offer little additional insight, and attention is focused here on the amplitude time series. Note that eddy amplitude and radius are not inversely correlated, so the observed eddy amplitude variations do not represent volume-conserving (mass conserving) combinations of horizontal contractions or expansions and compensating amplitude increases or decreases.

d. *Dynamical simulation*

For comparison with the observed eddy time series, the Chelton et al. (2011b) altimeter eddy identification and tracking procedure was applied to weekly SSH fields from a 7-year primitive equation numerical simulation of global ocean circulation (Maltrud and McClean 2005). While the total number of eddies is proportionally smaller than for the 19.5-year altimeter dataset, the simulated eddy life cycle, amplitude, and number distribution statistics otherwise closely match the observed altimeter-tracked eddy statistics. Both the mean-normalized amplitude and standard deviation cycles are quantitatively very close to the observed cycles (Fig. 2d). The simulated mean dimensional amplitudes at each lifetime are systematically larger than the observed, but have a similar dependence on lifetime, while the simulated number distribution is very similar to the observed (Fig. 4). The correspondence of these observed and simulated eddy statistics is consistent with the correspondence of observed and simulated mesoscale SSH variability reported by Fu (2009) for a similar global ocean model. An eddy census of a closely

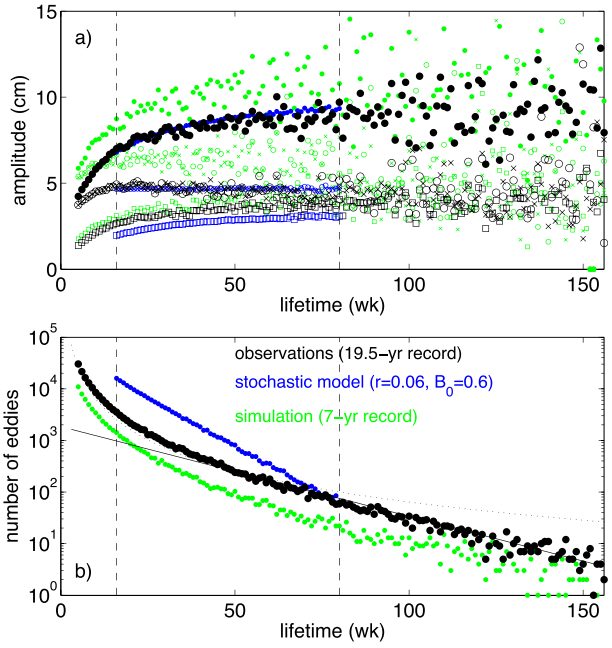

FIG. 4. (a) Dimensional-mean amplitude $\overline{A}^L$ (cm; filled circles) and std dev $\overline{A}^L\overline{S}^L$ (cm; empty squares) vs lifetime L for altimeter-tracked eddies for lifetimes $4 \le L \le 156$ weeks (black symbols). Also shown are the dimensional-mean initial (empty circles) and final (crosses) amplitudes. (b) Number of eddies vs lifetime for altimeter-tracked eddies (filled circles) for lifetimes L, $4 \le L \le 156$ weeks. Also shown are inverse-square power-law L^{-2} (dotted line) and exponential $\exp(-L/L_0)$ (solid line) distributions, with $L_0 = 25$ weeks. In both (a) and (b), corresponding quantities are also shown for the stochastic model with $r = 0.06$, $B_0 = 0.6$, and $\sigma = 1.82$ cm (blue) and dynamical simulation (green). In (b), the observational and dynamical simulation number distributions are nearly coincident when scaled by the ratio 19.5/7 of the lengths of the respective datasets.

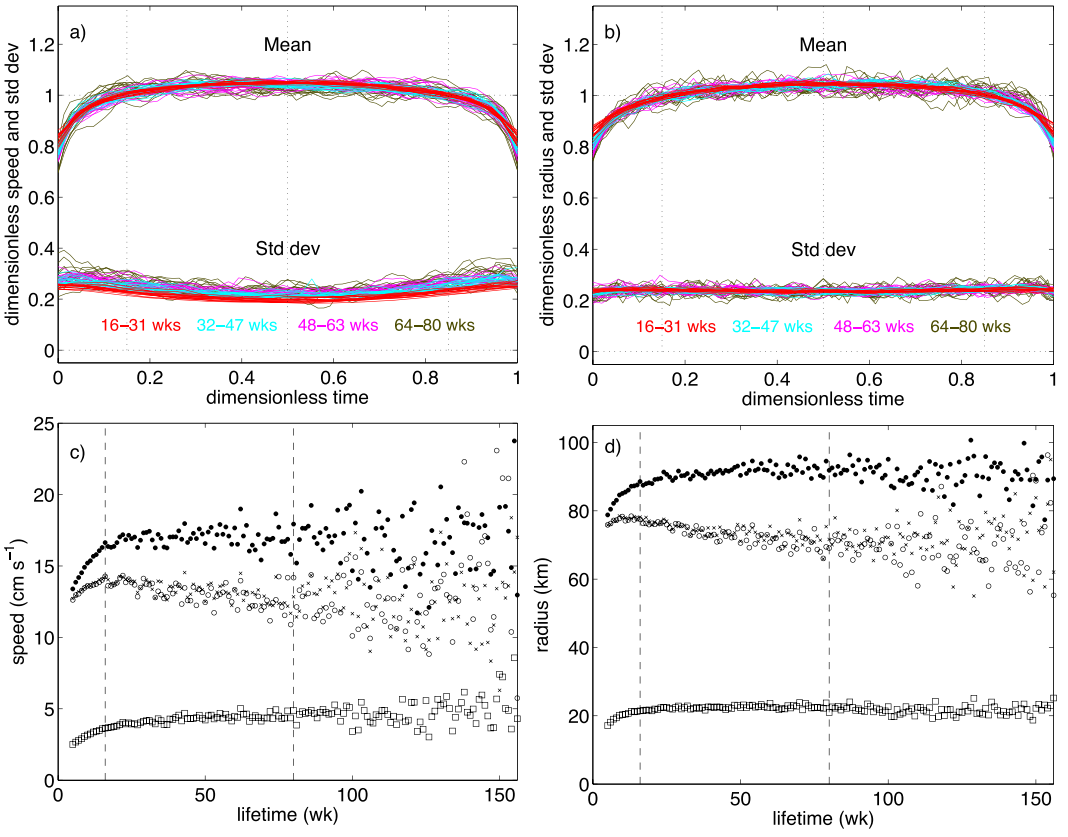

FIG. 5. Altimeter-tracked (a),(c) eddy fluid speed and (b),(d) radius-scale statistics: ensemble-mean and std dev time series (as in Fig. 2b) for normalized (a) fluid speed and (b) radius and dimensional mean (as in Fig. 4a) (c) speed and (d) scale vs lifetime.

related simulation based on the same numerical circulation model, using an alternative eddy detection algorithm, has recently been conducted by Petersen et al. (2013), and Dong et al. (2012) show temporal evolution of related mean-normalized eddy parameters from a regional model.

3. Stochastic model

a. A minimal model

The basic qualitative and quantitative properties, including time-reversal symmetry, approximate self-similarity, and uniformly negative curvature with respect to time, of the observed mean and standard deviation amplitude time series and distributions described in section 2 (Figs. 2–4) can be remarkably well reproduced with an extremely simple stochastic model. The minimal stochastic model is constructed in two steps: first, synthetic SSH time series are created for which the increments between successive time points are random numbers; second, these synthetic SSH time series are subjected to a simplified, thresholding analog of the Chelton et al. (2011b) altimeter eddy identification and tracking procedure.

Consider first a synthetic SSH anomaly time series $\{h(t_p);\ t_p = p\Delta t;\ p = 1, 2, 3, \ldots, P\}$ generated by a damped Gaussian random walk

$$h_\sigma(t_{p+1}) = h_\sigma(t_p) + \delta_p^\sigma - rh_\sigma(t_p) = \alpha h_\sigma(t_p) + \delta_p^\sigma, \quad (3.1)$$

where again $\Delta t = 1$ week, the random increment δ_p^σ is taken from a normal distribution with standard deviation σ, and r is the damping parameter, with $0 < \alpha = 1 - r < 1$. The standard deviation σ may be used to normalize the synthetic time series, so that $h = h_\sigma/\sigma$ satisfies

$$h(t_{p+1}) = h(t_p) + \delta_p - rh(t_p) = \alpha h(t_p) + \delta_p, \quad (3.2)$$

where again $\Delta t = 1$ week, $r = 1 - \alpha$ is a damping parameter with $0 < \alpha = 1 - r < 1$, and the random increment δ_p is taken from a normal distribution with unit standard deviation. Results for an increment distribution with standard deviation σ can be recovered from (3.2) by inverting the linear scaling:

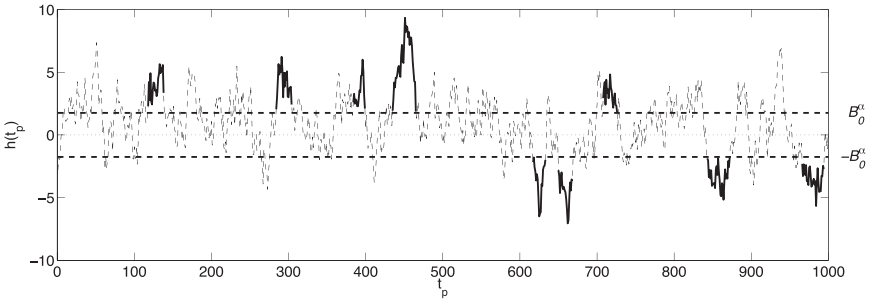

FIG. 6. Example 1000-week stochastic model synthetic SSH time series $\{h(t_p)\}$ (dashed line) vs time t_p (weeks), for $\alpha = 0.94$ and $B_0 = 0.6$ ($B_0^\alpha \approx 1.76$). The thresholds $\pm B_0^\alpha$ (thick dashed) and the corresponding synthetic eddy amplitude time series $\{A^m\}$ with lifetimes $L \geq 16$ weeks that are detected by the thresholding procedure (thick solid) are indicated. For this time series $\{h(t_p)\}$, there are five anticyclonic ($h > B_0^\alpha$) and four cyclonic ($h < -B_0^\alpha$) synthetic eddies that satisfy the criterion $L \geq 16$ weeks, and numerous other shorter-lived synthetic eddies that do not satisfy $L \geq 16$ weeks.

$$h_\sigma(t_p) = \sigma h(t_p). \tag{3.3}$$

The damped Gaussian random walk (3.2) is equivalent to a first-order autoregressive (AR1) Markov process and gives an asymptotically stationary distribution of normalized SSH values $\{h(t_p)\}$ with zero mean and standard deviation $\sigma_\alpha = (1-\alpha^2)^{-1/2}$ as $P \to \infty$ (Priestley 1987). Although the increments δ_p in (3.2) are uncorrelated in time, the resulting time series $\{h(t_p)\}$ has an autocorrelation time scale that is controlled by the parameter α (see section 4). The random increments δ_p should not be seen as a representation of additive observational noise, as the value of δ_p at time t_p will influence the values of $h(t_{p'})$ at all succeeding times $t_{p'} > t_p$ (to a successively lesser extent for increasing $t_{p'} - t_p$). Instead, the increments δ_p should be understood to represent physical changes in SSH anomaly.

The minimal stochastic model of eddy amplitude evolution is then obtained by subjecting a long synthetic SSH time series $\{h(t_p); j = 1, 2, \ldots, P\}$ from (3.2), or an ensemble of such series, to a threshold-based analog of the eddy identification and tracking procedure. An amplitude cutoff $B_0^\alpha = \sigma_\alpha B_0 > 0$ is chosen, and the existence of an SSH point with $|h(t_p)| > B_0^\alpha$ at time t_p in a given model time series is taken as an abstract analog of the identification by the automated algorithm of an eddy in the altimeter dataset at a specific location and time. A similar amplitude threshold is one of the criteria (see section 2a) used in the altimeter eddy identification algorithm (Chelton et al. 2011b). Each segment of the time series $\{h(t_p)\}$ for which $h(t_p) > B_0^\alpha$, or $h(t_p) < -B_0^\alpha$, for all t_p in a maximal interval $t_a \leq t_p \leq t_b$ is then identified as the eddy amplitude time series $\{A^m(t_j) = |h(t_p)|, t_j = t_p - t_a + \Delta t, t_a \leq t_p \leq t_b\}$ for a synthetic-tracked eddy with lifetime $L_m = t_b - t_a + \Delta t$ (Fig. 6).

The Chelton et al. (2011b) altimeter-based eddy dataset was obtained by applying an eddy detection procedure to a global, multiyear set of SSH fields to identify long-lived, coherent, localized eddy features. The eddy detection procedure itself consisted of two steps: identification of eddies in each weekly global SSH field and tracking of the identified eddies from week to week. The basic idea of the stochastic model is to represent both of these two elements: the underlying SSH variability, through (3.2), and the eddy detection procedure, through the thresholding at B_0^α. The definition of (3.2) yields synthetic SSH time series $\{h(t_p)\}$ that have a random walk character: the SSH value $h(t_p)$ at each time t_p depends both on the previous SSH value $h(t_{p-1})$ and on the random increment δ_{p-1}. At any given time step, the SSH value may increase or decrease with equal probability, but the resulting time series will wander between small and large amplitude on a slower mean time scale determined by α. The eddy identification step of the eddy detection procedure is represented by testing the magnitude of each SSH value $h(t_p)$: if $|h(t_p)| > B_0^\alpha$, a synthetic eddy is detected. The eddy tracking step is represented by finding the maximal interval $t_a \leq t_p \leq t_b$ during which either $h(t_p) > B_0^\alpha$ for all t_p (anticyclonic eddies) or $h(t_p) < -B_0^\alpha$ for all t_p (cyclonic eddies). Thus, if the SSH time series wanders across B_0^α toward larger amplitude, a synthetic eddy will be detected, and the lifetime of the synthetic eddy will depend on how long the wandering SSH amplitude stays above the threshold (Fig. 6). In this minimal stochastic model, there is no representation of the noise that exists in the altimeter data or of its effect on the eddy detection procedure. A refined model including additive noise is described below (section 3b). A heuristic, but more dynamically motivated, derivation of the basic SSH of (3.2) is also discussed below (section 5).

For the model analysis presented here, ensembles of $N = 5000$–$20\,000$ synthetic SSH time series $\mathcal{E} = \{h_n(t_p); n = 1, 2, \ldots, N; p = 1, 2, \ldots, P\}$ of length $P = 1000$ weeks were generated using (3.2), with initial 500-week segments first discarded to remove the effects of the ensemble initialization, for which values were drawn from a broad normal distribution. The values of N were chosen to provide a comparable number of model and observed eddies for lifetimes near 80 weeks. Ensemble-mean and standard deviation time series for these synthetic eddy amplitude time series were computed following (2.1) and (2.2). The optimal dimensional standard deviation σ for given model parameters was computed as the mean of the ratio of the dimensional observed amplitudes to the model amplitudes from (3.2) for lifetimes $16 \le L \le 80$ weeks, weighted by the number of altimeter-tracked eddies at each L. The threshold B_0^α was determined by setting B_0 to a value that gave approximate matches of model and observed eddy amplitude time series properties. The specification of B_0^α represents a subjective choice regarding the amplitude of features that are deemed sufficiently vigorous to be identified as eddies, reflecting the subjective elements of the Chelton et al. (2011b) eddy identification criteria summarized above (section 2a). Changing B_0^α will change the number and lifetimes of the synthetic eddies, and may cause eddy time series either to merge, if the threshold is lowered, or to split, if the threshold is raised.

For parameter values $r = 0.06$ ($\alpha = 0.94$; approximately equivalent to a 16-week e-folding decay time scale) and $B_0 = 0.6$, the ensemble of amplitude time series $\mathcal{E}^m = \{A^m\}$ constructed in this way, from (3.2) with the threshold B_0, reproduce most of the salient characteristics of the observed eddy amplitude time series. Ensemble-mean and standard deviation time series of normalized amplitude computed from $\mathcal{E}^m$ are time symmetric and have a time dependence that closely matches the observed series (Figs. 2c,d). The mean-normalized values of the initial and final amplitude points are accurately matched, and the midcycle flattening of the mean amplitude time series is partially reproduced. The mean standard deviations for this simplest stochastic model are 20% smaller than the observed mean standard deviations and do not show the weak midcycle minimum that is discernible in the observations (Figs. 2c,d); however, the model does qualitatively reproduce the observed decreases in standard deviations near the beginning and end of the series, as well as an observed modest increase in normalized standard deviation with increasing lifetime (Fig. 2c).

For the stochastic model [(3.2)] with $r = 0.06$ and $B_0 = 0.6$ and a corresponding objectively fitted dimensional standard deviation $\sigma = 1.82$ cm for (3.3), the stochastic model also reproduces basic aspects of the observed dimensional time- and ensemble-mean amplitude and standard deviation distributions (Fig. 4a). The mean amplitude is of comparable size (7–8 cm for $16 \le L \le 80$ weeks) and is similarly less dependent on lifetime with increasing lifetime. The dimensional-mean initial and final amplitudes are 4–5 cm, similar to the observed values, but have less lifetime dependence than the observed values, while, as already noted (Figs. 2b,c,d), roughly 80% of the standard deviation magnitude is represented. In addition, the model approximately reproduces the dependence of the observed eddy number distribution on lifetime, especially for the shorter lifetimes (Fig. 4b). The number distribution decays exponentially with lifetime L, with a uniform rate that is close to the mean observed rate in the range $16 \le L \le 80$ weeks, but lacks the curvature (in logarithm) of the observed distribution, which exhibits the transition noted previously from power law to exponential decay near $L = 40$ weeks. The parameter values $r = 0.06$ and $B_0 = 0.6$ were chosen to give a subjectively optimal overall fit of model results to the observations; different choices can give improved fits for specific quantities. The fitted value $\sigma = 1.82$ cm for $r = 0.06$ and $B_0 = 0.6$ corresponds to a dimensional threshold value $B_{0,\sigma} = \sigma B_0^\alpha = \sigma\sigma_\alpha B_0 \approx 3.2$ cm that is several times larger than the nominal 1-cm threshold in the observational SSH-based automated eddy identification procedure (Chelton et al. 2011b). However, the latter procedure includes four other quantitative criteria, the satisfaction of which is evidently represented here by the larger value for the single threshold–based model eddy identification criterion.

For the stochastic model with $r = 0.06$ (as in Figs. 2–4), the ensemble distribution $\mathcal{E}(t_p)$ of the original time series points at any fixed time $t = t_p$ is essentially normal, with mean zero and standard deviation $\sigma_\alpha = 2.93$ (Fig. 7a). The distributions of increments (first differences in time) from the normalized altimeter-tracked and $r = 0.06$, $B_0 = 0.6$ stochastic model eddy amplitude time series are both also nearly normal, with standard deviations 0.31 and 0.23, respectively, means and skewnesses near 0, and kurtoses near 3 (Fig. 7b). Note that the distribution of these synthetic eddy time series increments $A^m(t_{j+1}) - A^m(t_j)$ is not the same as the distribution of the random increments δ_p from the synthetic SSH anomaly time series $\{h(t_p)\}$, because the eddy time series $\{A^m\}$ are a set of thresholded and normalized subsequences of the SSH time series. With B_0 fixed, decreasing r gives stronger dependence of dimensional-mean amplitude on lifetime, smaller dimensionless standard deviations and increments, and more longer lifetime eddies, while increasing r has the opposite effects (Fig. 8). With r fixed, decreasing B_0 also gives stronger dependence of the

dimensional-mean amplitude on lifetime, but reduces the dimensionless and dimensional initial and final amplitude values and gives larger dimensionless increments, while having relatively little effect on the eddy number distribution (Fig. 8). Pure noise ($\alpha = 0$) calculations were also conducted. These had the anticipated flat ensemble-mean amplitude behavior over the central portion of the cycle, with abrupt transitions near the final and initial points, rather than the observed smooth transitions; the associated number distributions were inconsistent with the observations in that the number of synthetic eddies decreased exponentially with lifetime at a much more rapid rate than observed.

Mathematical results for the excursions of random walks past thresholds, such as these synthetic eddy amplitude time series, do not appear to be available, although many results have long been known for the related problem of one-sided (in time) escapes from intervals or past thresholds, such as the well-known gambler's ruin (Spitzer 1976; Ibe 2009; Lawler and Limic 2010). Heuristic explanations of the ensemble-mean amplitude time series structure may be offered for two extreme cases: series with only three time points and series that are very long relative to the decay time scale associated with α. In the latter case, the series should approach pure white noise, except near the initial and final points, and the central portion of the ensemble-mean amplitude and standard deviation cycles should be constant at values that depend on the threshold but not the lifetime. In the former case, the initial and final amplitudes are constrained to relatively small values by the adjacent threshold crossings, while the midpoint amplitude is constrained to a larger value by the absence of adjacent threshold crossings, which gives the characteristic negative curvature of the ensemble-mean series. It is unclear whether the intermediate length series examined here represent interpolations between these two extremes or a distinct regime with intrinsic scaling. It was further unexpected to find time-reversal symmetry for series as long as 5 times the 16-week decay time scale associated with $\alpha = 0.94$. Exploratory calculations indicate that the time-reversal symmetry is easily broken by nonnormal, random increment distributions with rare large increments, as the latter can be balanced by weak damping only if they occur near the beginning of the life cycle.

b. Noise and smoothing

The maximally simple stochastic model formulation (3.2)–(3.3) described in section 3 does not contain an explicit representation of noise in the observed signal nor of the space–time smoothing associated with the optimal interpolation procedure by which the gridded altimeter dataset is produced from along-track altimetric time

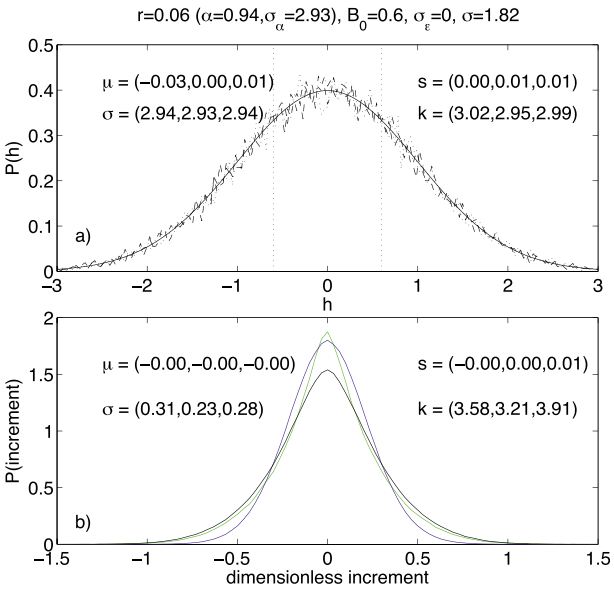

FIG. 7. (a) Distributions of stochastic model time series ensemble $\mathcal{E} = \{h_n(t_p);\ n = 1, 2, \ldots, N\}$ for $N = 20\,000$ at the fixed times $t_p, p = (1, 500, \text{and } 1000)$ (dashed, dashed–dotted, and dotted lines) for $r = 0.06$ (as in Fig. 2c). An initial sequence of 500 iterates prior to t_1 has been discarded, so that the resulting distribution is statistically stationary. The normal distribution with zero mean and std dev $\sigma_\alpha = 2.93$ (solid) is also shown, and the threshold values $|h| = B_0 = 0.6$ (vertical dotted) are indicated. (b) Distributions of increments (first differences in time) from time series of a normalized altimeter-tracked (black), stochastic model with $r = 0.06$, $B_0 = 0.6$ (blue) and dynamical simulation (green) eddy amplitudes. In both panels, the corresponding means μ, std dev σ, skewnesses s, and kurtoses k of these distributions are shown.

series; a summary of the latter is provided by Chelton et al. (2011b). The stochastic model can be modified to include a random-noise component to the original stochastic ensemble time series from (3.2), according to

$$h^{\varepsilon}(t_p) = h(t_p) + \varepsilon_p, \tag{3.4}$$

where ε_p is a random number drawn from a normal distribution with standard deviation σ_ε. Note that the noise component ε_p is added to the time series points $h(t_p)$ after the construction of the time series using (3.2) and is uncorrelated in time. The analog eddy identification and tracking through the threshold B_0 is then carried out on the ensemble $\mathcal{E}^{\varepsilon} = \{h^{\varepsilon}\}$ of the time series with additive noise. Improved agreement of the stochastic model standard deviation time series with the observed series can be obtained using the noise model (3.4) with $r = 0.06$ and $\sigma_\varepsilon = 0.5$, for which a threshold $B_0 = 0.37$ gives comparable agreement of the ensemble-mean model series with the observed series (Fig. 9a). The fitted dimensional standard deviation for this case is $\sigma = 2.04$ cm, corresponding to a dimensional threshold

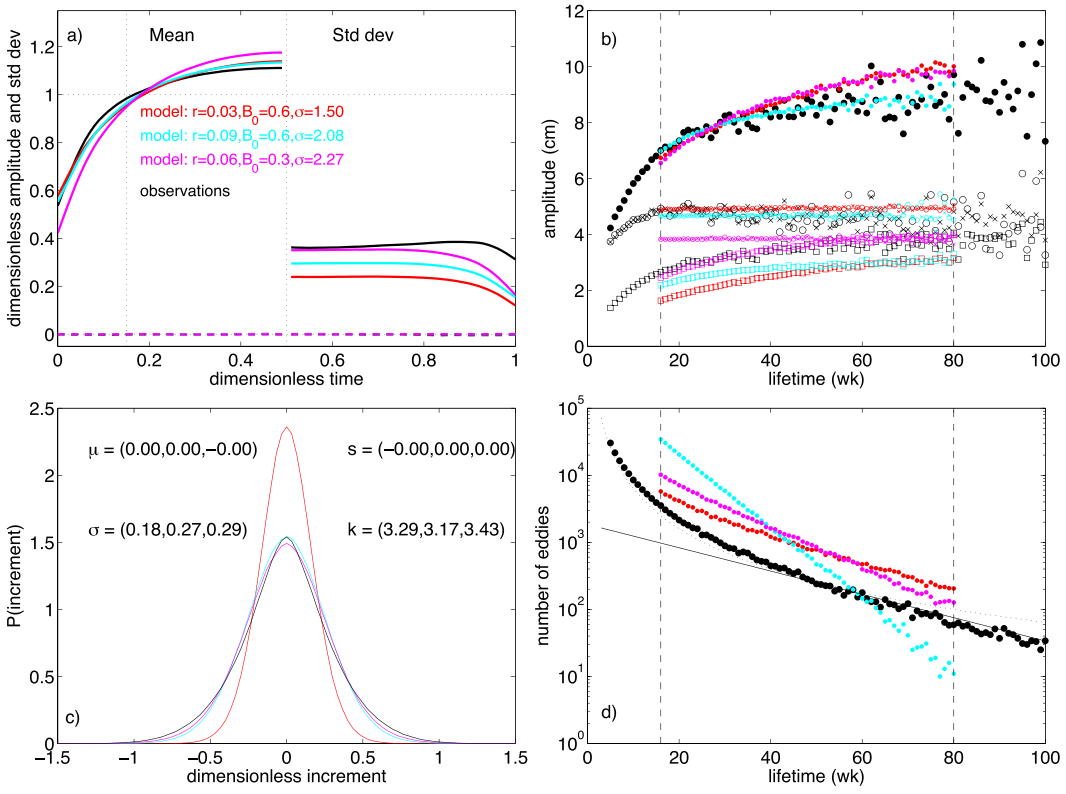

FIG. 8. Model results with (i) $r = 0.03(\alpha = 0.97)$, $B_0 = 0.6$, and $\sigma = 1.50$ cm; (ii) $r = 0.09(\alpha = 0.91)$, $B_0 = 0.6$, and $\sigma = 2.08$; and (iii) $r = 0.06(\alpha = 0.94)$, $B_0 = 0.3$, and $\sigma = 2.27$. (a) As in Fig. 2d. (b) As in Fig. 4a. (c) As in Fig. 7b. (d) As in Fig. 4b.

$B_{0,\sigma} = \sigma B_0^{\alpha} = \sigma\sigma_{\alpha} B_0 \approx 2.2$ cm and a dimensional noise standard deviation $\sigma\sigma_{\varepsilon} \approx 1$ cm, somewhat smaller than a typical error estimate for the AVISO Reference Series (Ducet et al. 2000). This solution gives an increment standard deviation of 0.32 for the dimensionless time series, which nearly matches the standard deviation of the increment distribution of the observed normalized amplitude time series, although the distribution shapes are not identical (Figs. 7b, 9c).

Improved agreement of the stochastic model–mean amplitude time series with the observed series can be obtained by smoothing the noise model time series from (3.4). The smoothing procedure used here is an 11-point Gaussian filter with decay time scale s_t:

$$h^s(t_p) = \sum_{k=-5}^{5} c_k h^{\varepsilon}(t_{p+k}),$$

$$c_k = C_0 \exp[-(k\Delta t)^2/2s_t^2], \quad \text{and}$$

$$C_0 = \left(\sum_{k=-5}^{5} c_k \right)^{-1}. \tag{3.5}$$

The analog eddy identification and tracking through the threshold B_0 is then carried out on the ensemble $\mathcal{E}^s = \{h^s\}$ of smoothed-noise time series. For the parameter choice $r = 0.04$ ($\alpha = 0.96$; approximately equivalent to a 24-week decay time scale), $B_0 = 0.48$, $\sigma_{\varepsilon} = 1.75$, and $s_t = 0.8$ weeks, with fitted standard deviation $\sigma = 1.50$ cm, the mean amplitude life cycle produced by the modified smoothed-noise stochastic model, (3.2) with (3.4) and (3.5), shows improved agreement with the observed mean cycle (Fig. 9a). The model and observed standard deviations from the mean cycle are again close, as are the model and observed increment distributions (Fig. 9). The number distribution versus lifetime for the smoothed-noise model also shows an improved agreement with the observed distribution, as the curvature of the observed distribution is partially reproduced. For this case, the dimensional threshold $B_{0,\sigma} \approx 2.6$ cm, and the dimensional noise standard deviation $\sigma\sigma_{\varepsilon} \approx 2.6$ cm.

For the parameter choice $r = 0.03$ ($\alpha = 0.97$; approximately equivalent to a 32-week decay time scale), $B_0 = 0.61$, $\sigma_{\varepsilon} = 2.5$, and $s_t = 1.3$ weeks, with fitted standard deviation $\sigma = 1.36$ cm, the mean amplitude life cycle produced by the modified smoothed-noise stochastic model, (3.2) with (3.4) and (3.5), is essentially indistinguishable from the observed mean cycle (Fig. 9a). The standard deviations from the mean cycle are larger

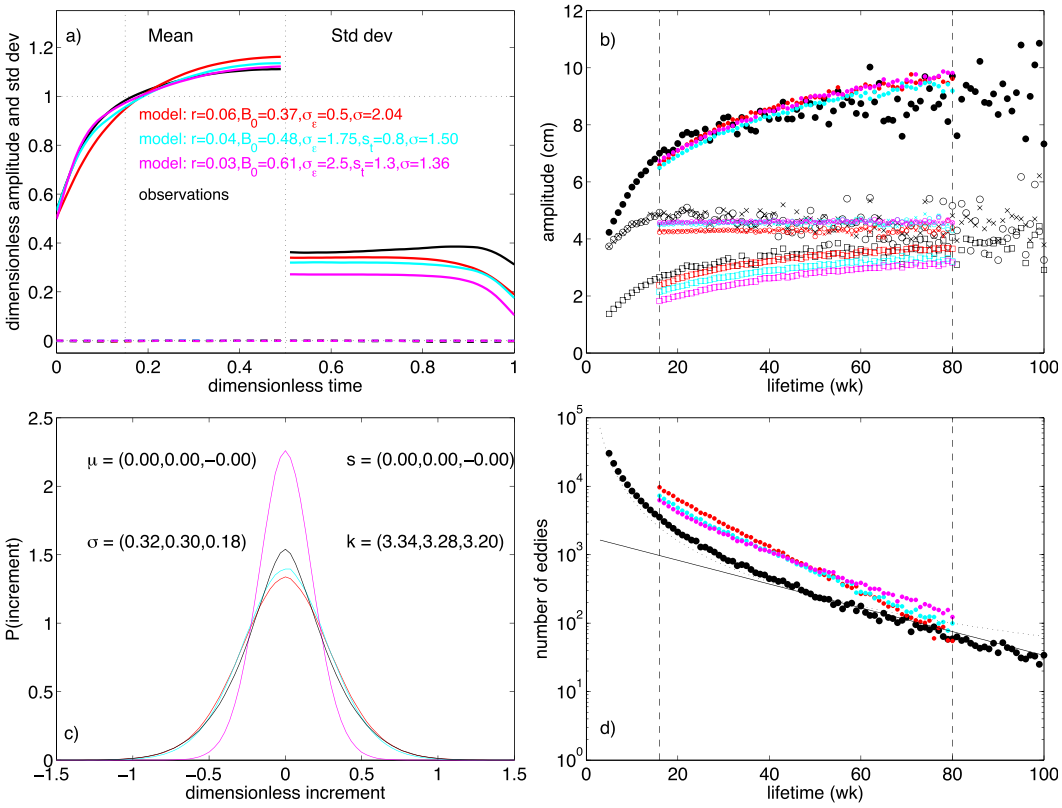

FIG. 9. Model results with (i) $r = 0.06(\alpha = 0.94), B_0 = 0.37, \sigma_\varepsilon = 0.5$, and $\sigma = 2.04$ cm; (ii) $r = 0.04(\alpha = 0.96)$, $B_0 = 0.48, \sigma_\varepsilon = 1.75$, 11-point Gaussian smoothing with $s_t = 0.8$, and $\sigma = 1.5$; (iii) $r = 0.03(\alpha = 0.97), B_0 = 0.61$, $\sigma_\varepsilon = 2.5$, 11-point Gaussian smoothing with $s_t = 1.3$, and $\sigma = 1.36$. (a) As in Fig. 2d. (b) As in Fig. 4a. (c) As in Fig. 7b. (d) As in Fig. 4b.

than for the original stochastic model (3.2) without noise or smoothing (Fig. 2), but are now only approximately three-fourths as large as the observed standard deviations (Figs. 9a,b). The number distribution versus lifetime for the smoothed-noise model shows good agreement with the observed distribution, as the curvature of the observed distribution is again partially reproduced (Fig. 9d). However, the agreement of the model and observed increment distributions is substantially degraded relative to the simpler model, as the standard deviation of the smoothed-noise increments is reduced from 0.23 to 0.18, roughly half of the observed value of 0.31 (Fig. 9c). The dimensional value of the noise standard deviation for this case is $\sigma\sigma_\varepsilon = 3.4$ cm, equal to the dimensional threshold $B_{0,\sigma} = 3.4$ cm and to a typical error estimate for the AVISO Reference Series (Ducet et al. 2000).

4. SSH autocorrelation structure

The comparisons (Figs. 2–4) of the thresholded stochastic model and observed eddy amplitude time series suggest an optimal value $\alpha = 0.94$ ($r = 1 - \alpha = 0.06$) for the AR1 parameter in (3.2). The autocorrelation function of the original AR1 time series $\{h(t_p)\}$ from (3.2) is then $\alpha^{t_p} = (0.94)^{t_p}$. The latter can be compared to empirical autocorrelation functions (ACF) computed directly from the 19.5-year altimeter SSH dataset from which the observed eddy amplitude time series were extracted through application of the Chelton et al. (2011b) eddy identification and tracking procedure. If the autocorrelations are computed from the SSH dataset by combining SSH observations along planetary wave characteristics, the results for latitudes 20°–40°N and 20°–40°S are closely consistent with the model value $\alpha = 0.94$ (Fig. 10). Planetary wave characteristics for this calculation were defined as $x(t) = x_0 + c_R t$, where x is longitude, x_0 is initial longitude, t is time, and $c_R < 0$ is the average long planetary wave speed computed following Killworth et al. (1997). This agreement is robust: similar agreement is found for most lags between 3 and 20 weeks (Fig. 11), and rest state values of c_R could equally well be used.

If the autocorrelations are computed instead from SSH observations at fixed longitudes (i.e., along effective

characteristics with $c_R = 0$), the resulting decorrelation scales are much shorter at all latitudes equatorward of 45°N and 45°S (Fig. 10); presumably this rapid decorrelation results from the propagation past fixed longitudes, at speeds near c_R, of a spatially random mesoscale SSH field that, in contrast, is seen to evolve much more slowly along c_R characteristics. Thus, not only does the thresholded stochastic ensemble $\mathcal{E}^m$ provide a good model of the observed eddy amplitude life cycles, but the damped stochastic process (3.2) combined with deterministic long Rossby wave propagation also provides a good model for the evolution of the underlying SSH field. The stochastic model is thus able to represent the observed statistics both before and after the application of the eddy identification and tracking algorithm, and consequently the observed eddies may be consistently interpreted as the large-amplitude excursions of a damped stochastic process.

A related maximum-lagged cross-correlation approach has been used by Fu (2009) to estimate propagation characteristics from AVISO SSH data empirically. The frequency spectrum $S(\omega)$ of the Gaussian AR1 process with parameter α is proportional to $1/(\omega_\alpha^2 + \omega^2)$, where $\omega_\alpha = -\ln\alpha$; the autocorrelation, or slowly varying character, of the AR1 variable can be seen as a consequence of the redness of this spectrum $S(\omega)$. The refined stochastic models (3.4) and (3.5) suggest larger values for the parameter α and thus longer intrinsic physical decorrelation times for SSH on long planetary wave characteristics, which may seem inconsistent with this previous comparison. However, these refined models include separate representations of noise and smoothing processes that are included in the observed, gridded SSH fields from which the empirical autocorrelation functions were computed. Thus, the empirical autocorrelation functions from the observed, gridded SSH fields should not be compared directly to autocorrelation functions associated with the values of α inferred for the refined stochastic models (3.4) and (3.5).

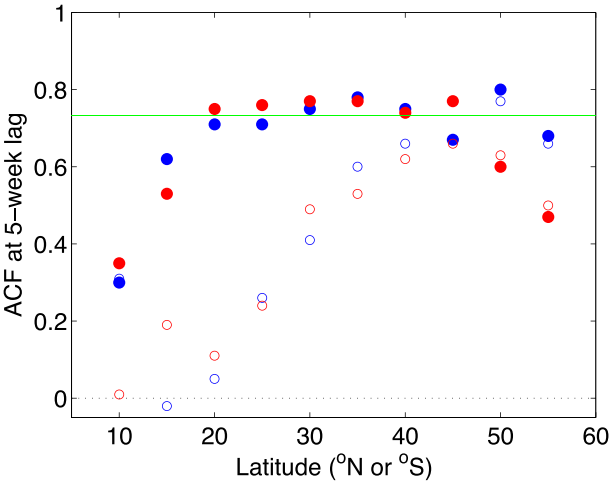

FIG. 10. Mean autocorrelation at 5-week lag of altimeter SSH along linear planetary wave characteristics (filled circles) and at fixed lon (open circles) for the North (blue) and South (red) Pacific vs lat for lon 180°–130°W (North Pacific) and 170°–120°W (South Pacific). Also shown is the autocorrelation at 5-week lag $\alpha^5 = (0.94)^5 \approx 0.73$ for an AR1 process with $\alpha = 0.94$ (green solid line).

5. Heuristic derivation of stochastic model

The abstract stochastic model (3.1) of the evolution of SSH anomalies may be obtained heuristically as a time-discretized dynamical model in the linear, long-wave regime. Consider a dimensional, forced, damped, linear, long-wave, reduced gravity, and quasigeostrophic potential vorticity equation of the form

$$\frac{\partial}{\partial t}\left(-\frac{1}{\lambda^2}\psi\right) + \beta\frac{\partial\psi}{\partial x} = \frac{f_0}{H_0}W_E - \mathcal{D}, \tag{5.1}$$

where λ is the internal deformation radius; $\psi(x, y, t)$ is the velocity streamfunction; f_0 and β are the local value and meridional gradient of the Coriolis parameter, respectively; H_0 is the undisturbed depth of the active layer; W_E is an Ekman pumping velocity; and $\mathcal{D}$ is a dissipative term. With the substitution $\psi = (g/f_0)\eta$, where $\eta(x, y, t)$ is the SSH anomaly and g is the effective acceleration of gravity, (5.1) may be written

$$\frac{\partial\eta}{\partial t} + \beta\lambda^2\frac{\partial\eta}{\partial x} = F_t - R\eta, \tag{5.2}$$

where now $F_t = (\Delta\rho/\rho_0)W_E$ will be taken to be the derivative of a Brownian motion, with $\Delta\rho/\rho_0 = \lambda^2 f_0^2/(gH_0)$ representing the fractional density difference between the active layer and the deep resting layer, and a specific form has been chosen for $\mathcal{D}$, with R^{-1} as the corresponding decay time scale.

We can integrate (5.2) from $t = t_p$ to $t = t_{p+1} = t_p + \Delta t$ along the long-wave characteristic $x(t) = x_0 + c_R t, y(t) = y_0$, where $c_R = -\beta\lambda^2$ in this simplified derivation that neglects mean flow effects, to obtain

$$\begin{aligned}\eta(t_{p+1}; x_0) &= \eta(t_p; x_0) + \Delta t\delta_p^F - R\int_{t_p}^{t_{p+1}} \eta[t; x(t)]\, dt \\ &\approx (1 - \Delta t R)\eta(t_p; x_0) + \Delta t\delta_p^F .\end{aligned} \tag{5.3}$$

In (5.3), $\eta(t; x_0) = \eta[x(t), y_0, t]$, δ_p^F is the standard deviation of the Gaussian random increment for F_t, and an Euler forward step has been used in the final expression to approximate the integral of the damping term. The two equations (5.3) and (3.1) are identical if the definitions

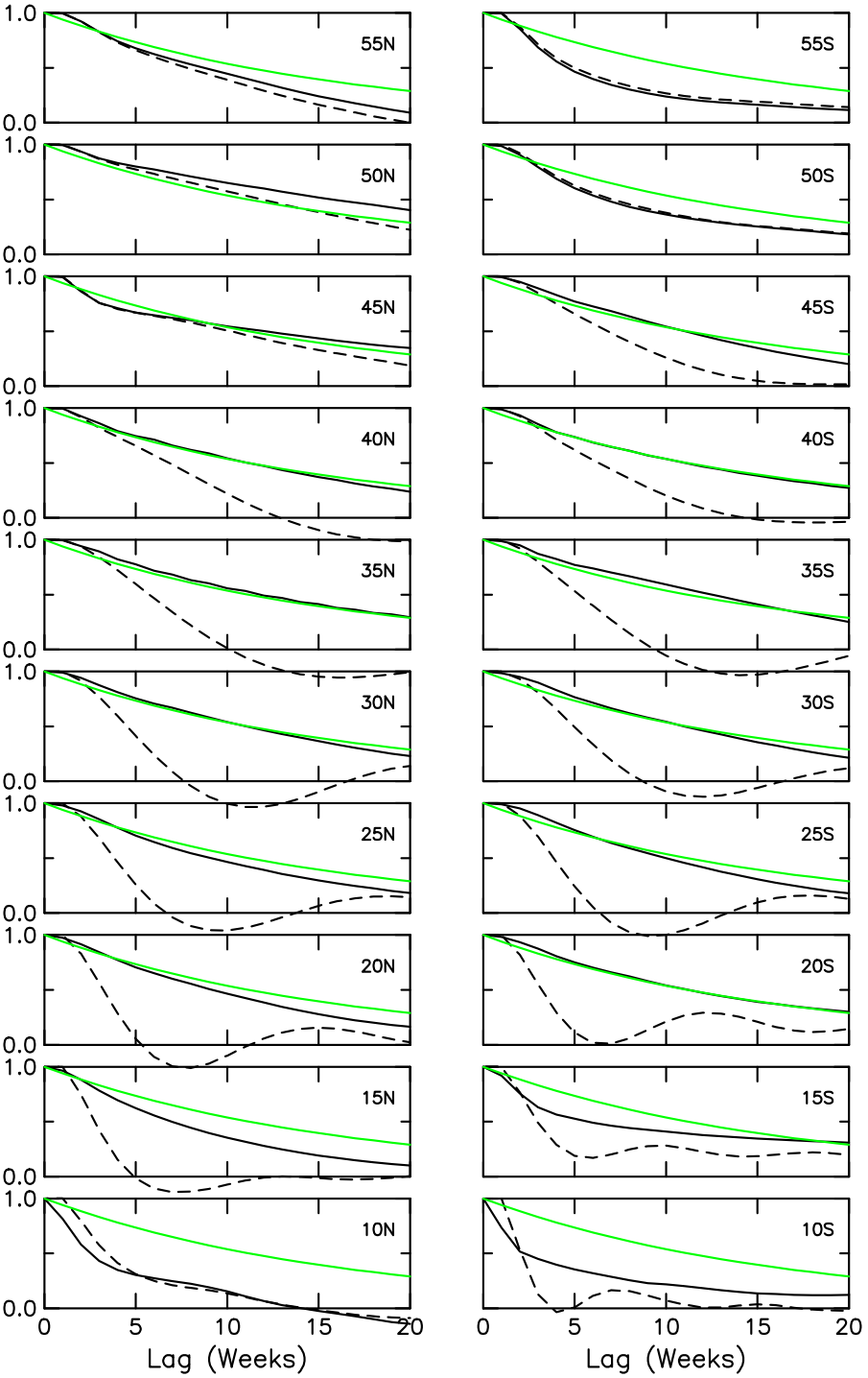

FIG. 11. Mean autocorrelation vs lag for altimeter SSH along linear planetary wave characteristics (black solid line) and at fixed lon (black dashed line) for the (left) North and (right) South Pacific at 5° lat increments in 10°–50°N and 10°–50°S for lon 180°–130°W (North Pacific) and 170°–120°W (South Pacific). Also shown is the autocorrelation α^t for an AR1 process with $\alpha = 0.94$ and time t (weeks; green).

$$h_\sigma(t_p) = \eta(t_p; x_0), \quad \delta_p^\sigma = \Delta t \delta_p^F, \quad \text{and} \quad r = \Delta t R \tag{5.4}$$

are made. The random increment δ_p^F may be taken to be drawn from a normal distribution with standard deviation $\sigma^F = (\Delta\rho/\rho_0)\sigma^{W_E}$, where σ^{W_E} is the corresponding standard deviation of the dimensional Ekman pumping. The relation for σ^{W_E} gives a dimensional estimate for the equivalent wind-forcing amplitude that would be required to match the amplitude of the random increments in the stochastic model:

$$\sigma^{W_E} = \frac{\rho_0}{\Delta\rho}\frac{\sigma}{\Delta t} = 10^3 \times \frac{1.82\,\text{cm}}{1\,\text{week}} \approx 3 \times 10^{-5}\,\text{m s}^{-1} \approx 10^3\,\text{m yr}^{-1}. \tag{5.5}$$

For Ekman pumping σ^{W_E} from wind stress curl over a horizontal scale $l_\tau = 100$ km, comparable to the mean radius of the tracked eddies (Chelton et al. 2011b), this requires wind stress anomalies of order $\Delta\tau_* = \rho_0 f_0 l_\tau \sigma^{W_E} \approx 0.3\,\text{N m}^{-2}$, corresponding to wind speed anomalies of order $U_a = [\Delta\tau_*/(\rho_a C_D)]^{1/2} = [0.3\,\text{N m}^{-2}/(1\,\text{kg m}^{-3} \times 10^{-3})]^{1/2} \approx 20\,\text{m s}^{-1}$. As estimates of typical midlatitude open-ocean wind forcing on 100-km scales, these values of Ekman pumping, wind stress curl, and wind speed anomalies are unrealistically large, indicating that the random increments in the stochastic model cannot generally be interpreted as wind forcing and must instead be understood to represent internal dynamical interaction processes. The stochastic model-damping time scales from 16 ($r = 0.06$) to 32 ($r = 0.03$) weeks are more similar to but still shorter than estimates for eddy decay from surface current–induced Ekman pumping (McGillicuddy et al. 2007, 2008; Eden et al. 2009; Gaube 2012), indicating that the linear decay term also must represent other internal dynamical effects that systematically reduce eddy amplitudes.

It is important to recognize that, while the observed eddies do propagate at speeds close to the linear wave speed c_R (Chelton et al. 2011b), the preceding heuristic derivation of (5.3) can serve only as informal motivation for the stochastic model (3.1), because the restriction of (5.1) to the linear, long-wave regime is inconsistent with the observational evidence for the nonlinearity of the observed eddies and with the range of horizontal scales resolved by the observations, which extends to scales roughly equal to midlatitude values of the deformation radius λ. For the case of stochastic wind forcing, linear equations related to (5.2) have been previously considered by Müller and Frankignoul (1981), Brink (1989), Samelson (1990), and others. However, the estimate (5.5) demonstrates that the amplitude of the stochastic forcing in the present model is much too large to be interpreted physically as wind forcing, so the implied dynamics of the stochastic model (3.1) are fundamentally different from those previous wind-forced models. A more rigorous derivation of the stochastic model from nonlinear dynamical equations may be possible using homogenization arguments (e.g., Franzke and Majda 2006).

6. Discussion and conclusions

Two fundamental conclusions regarding the nature, in this global-mean context, of mesoscale ocean turbulence follow from these results. The first is that the evolution of mesoscale structures is dominated by effectively stochastic interactions, rather than by the classical wave-mean cycle of initial growth through mean flow instability followed by nonlinear equilibration and barotropic, radiative, or frictional decay, or by the vortex merger processes of inverse turbulent cascade theory; a more general consistency with geostrophic turbulence theory is still possible. The second is that the underlying stochastic description applies to the full observed SSH anomaly field itself, when the latter is viewed on long planetary (Rossby) wave characteristics, so that the nonlinear ocean eddies detected by the eddy identification and tracking procedure may be appropriately viewed as large-amplitude excursions of the same effectively stochastic process.

A long history of dynamical theory suggests that the main source for open-ocean eddies is baroclinic instability of the large-scale flow (Gill et al. 1974; Robinson and McWilliams 1974; Rhines 1975; Spall 2000; Smith 2007; Tulloch et al. 2011), and this is likely true for many or most of the altimeter-tracked eddies considered here. However, the basic structure of the observed eddy amplitude life cycles (Fig. 2b) differs fundamentally from that which would be expected on the basis of classical interpretations of ocean eddy evolution as a mean flow instability process following a simple growth–equilibration–decay cycle, in which the exponential growth time scale in the linear regime depends on an appropriate measure of supercriticality of the mean flow, not on the lifetime of the resulting eddy. Likewise, eddy decay driven by frictional (Arbic and Flierl 2004), radiative (McWilliams and Flierl 1979), or barotropization (Smith and Vallis 2002) processes should have time scales proportional, respectively, to frictional parameters or to energy transmission or conversion rates, which are not intrinsically related to the lifetime of the eddy. The uniformly negative curvature of the time series further excludes the possibility of an initial period of exponential growth, for which a positive curvature of the time series would be found, although an initial exponential growth phase might still exist prior to detection of the eddies by

the closed SSH contour algorithm. The observed time-reversal symmetry is inconsistent with the irreversible vortex merger phenomenology of inverse quasigeostrophic turbulent cascades (Rhines 1977; McWilliams 1984) and also differs from what would be anticipated from classical interpretations of ocean eddies in terms of simple wave-mean flow life cycles, in which instability growth and the frictional, radiative, or barotropization decay processes have dynamically independent time scales that would produce life cycles with time-reversal symmetry only through extraordinary coincidence. This does not exclude the possible existence of specific regional regimes or individual eddies that do show a simpler, more classical, growth–equilibration–decay eddy life cycle; the conclusions here relate to the mean statistical behavior for the entire global altimeter-based eddy dataset.

Physical interpretation of the amplitude of the stochastic model random increment as external forcing requires a conversion to equivalent direct wind-driven Ekman pumping, the dominant external forcing of the open ocean under most circumstances (Gill 1982). The conversion factor can be obtained through a partially heuristic derivation (section 5) of the stochastic model from a forced–damped quasigeostrophic potential vorticity equation. For the basic stochastic model with $r = 0.06$, $\sigma = 1.82\,\mathrm{cm}$, and time step $\Delta t = 1$ week, this yields an equivalent dimensional Ekman pumping standard deviation σ^{W_E} of order $10^3\,\mathrm{m\,yr^{-1}}$. For Ekman pumping from wind stress curl over a horizontal scale comparable to the mean radius of the tracked eddies, this requires unrealistically large wind stress and speed fluctuations of order $0.3\,\mathrm{N\,m^{-2}}$ and $20\,\mathrm{m\,s^{-1}}$, which occur only infrequently in the midlatitude oceans. The stochastic model damping time scale of 16 weeks for $r = 0.06$ ($\alpha = 0.94$) is short relative to most estimates of eddy decay from frictional processes, but presumably also parameterizes any systematic tendency for breakdown of coherent eddy structures through hydrodynamical instabilities, eddy–eddy interactions, and other internal dynamical mechanisms. Refined stochastic models that include representations of observational noise give somewhat longer decay time scales, but these are still shorter than typical estimates for decay from processes such as surface current–induced Ekman pumping (McGillicuddy et al. 2007, 2008; Eden et al. 2009; Gaube 2012). Consequently, the random increments in the stochastic model and, in part, the frictional decay term must both be interpreted physically not as external forcing, but instead as representations of internal dynamical processes, including interactions between different elements of the ocean flow field. These may take the form, for example, of eddy-mean, eddy–eddy, or eddy–wave interactions, as well as radiative, barotropization, and vortex merger and instability processes. These interactions might further be envisioned to include, for example, exchanges between eddies—or between an eddy and the ambient turbulent field—of fluid and of a materially advected potential vorticity. Additional analysis of the tracked eddy dataset may offer insight into the mechanisms of these interactions.

Previous theoretical interpretations of mesoscale dynamics have spanned the range from forced linear wave theory (Müller and Frankignoul 1981) through baroclinic instability (Gill et al. 1974) to fully developed geostrophic turbulence (Rhines 1977). Coherent eddies have been identified as end states of vortex mergers in freely decaying, inviscid quasigeostrophic turbulence (McWilliams 1984) and punctuated, Hamiltonian, point vortex models allowing that vortex mergers have been successful in simulating aspects of such flows (Carnevale et al. 1991; Weiss 1999), but the dynamics and role of coherent eddies under statistically stationary conditions in which their amplitudes fluctuate continuously, decreasing and increasing with equal probability, are unclear. This random fluctuation behavior appears qualitatively more akin to the momentum dynamics of elastic scattering of molecules in an ideal gas than to standard views of unidirectional energy cascades and vortex interactions in quasi-two-dimensional geophysical turbulence, although the mechanisms of amplitude increase and decrease have not been identified and may involve eddy-mean as well as eddy–eddy interactions. The random fluctuation life cycles may still be consistent with the existence of geostrophic turbulence and an associated inverse energy cascade, if the cascade flux is sufficiently weak relative to the general turbulent mesoscale activity; such a consistency would seem necessary if the analyzed dynamical simulation (section 2d) contains a geostrophic turbulence process. The global observations by Chelton et al. (2011b) raise fundamental questions regarding the role and existence of persistent nonlinear eddies in the turbulent ocean mesoscale: for example, do these eddies mediate, interrupt, or arise from the inverse energy cascade that has been predicted to occur in homogeneous geostrophic turbulence? The present results do not immediately suggest direct answers to these subtle and far-reaching questions, but, by providing a novel, succinct, quantitative model of mesoscale variability, offer a new and promising path toward dynamical understanding of this energetic, ubiquitous, and broadly important ocean regime.

Acknowledgments. This research was funded as part of the National Aeronautics and Space Administration (NASA) Ocean Surface Topography Mission through NASA Grants NNX08AR37G and NNX13AD78G.

REFERENCES

Anderson, L., D. McGillicuddy, M. Maltrud, I. Lima, and S. Doney, 2011: Impact of eddy–wind interaction on eddy demographics and phytoplankton community structure in a model of the North Atlantic Ocean. *Dyn. Atmos. Oceans,* **52,** 80–94.

Arbic, B. K., and G. R. Flierl, 2004: Baroclinically unstable geostrophic turbulence in the limits of strong and weak bottom Ekman friction: Application to midocean eddies. *J. Phys. Oceanogr.,* **34,** 2257–2273.

Bretherton, F. P., 1966: Critical layer instability in baroclinic flows. *Quart. J. Roy. Meteor. Soc.,* **92,** 325–334.

Brink, K. H., 1989: Evidence for wind-driven current fluctuations in the western North Atlantic. *J. Geophys. Res.,* **94** (C2), 2029–2044.

Carnevale, G. F., J. C. McWilliams, Y. Pomeau, J. B. Weiss, and W. R. Young, 1991: Evolution of vortex statistics in two-dimensional turbulence. *Phys. Rev. Lett.,* **66,** 2735–2737.

Chelton, D. B., and M. G. Schlax, 1996: Global observations of oceanic Rossby waves. *Science,* **272,** 234–238.

——, P. Gaube, M. G. Schlax, J. J. Early, and R. M. Samelson, 2011a: The influence of nonlinear mesoscale eddies on oceanic chlorophyll. *Science,* **334,** 328–332.

——, M. G. Schlax, and R. M. Samelson, 2011b: Global observations of nonlinear mesoscale eddies. *Prog. Oceanogr.,* **91,** 167–216, doi:10.1016/j.pocean.2011.01.002.

Collins, C. A., T. Margolina, T. A. Rago, and L. Ivanov, 2013: Looping RAFOS floats in the California Current System. *Deep-Sea Res. II,* **85,** 42–61.

Dantzler, H. L., 1977: Potential energy maxima in the tropical and subtropical North Atlantic. *J. Phys. Oceanogr.,* **7,** 512–519.

Dong, C., and Coauthors, 2012: Three-dimensional oceanic eddy analysis in the Southern California Bight from a numerical product. *J. Geophys. Res.,* **117,** C00H14, doi:10.1029/2011JC007354.

Ducet, N., P.-Y. Le Traon, and G. Reverdin, 2000: Global high resolution mapping of ocean circulation from TOPEX/POSEIDON and *ERS-1/2*. *J. Geophys. Res.,* **105** (C8), 19 477–19 498.

Early, J. J., R. M. Samelson, and D. B. Chelton, 2011: The evolution and propagation of quasigeostrophic ocean eddies. *J. Phys. Oceanogr.,* **41,** 1535–1555.

Eden, C., H. Dietze, and D. Weg, 2009: Effects of mesoscale eddy/wind interactions on biological new production and eddy kinetic energy. *J. Geophys. Res.,* **114,** C05023, doi:10.1029/2008JC005129.

Franzke, C., and A. J. Majda, 2006: Low-order stochastic mode reduction for a prototype atmospheric GCM. *J. Atmos. Sci.,* **63,** 457–479.

Fu, L.-L., 2009: Pattern and velocity of propagation of the global ocean eddy variability. *J. Geophys. Res.,* **114,** C11018, doi:10.1029/2009JC005349.

Gaube, P., 2012: Satellite observations of the influence of mesoscale ocean eddies on near-surface temperature, phytoplankton and surface stress. Ph.D. thesis, Oregon State University, 197 pp. [Available from Oregon State University, 104 CEOAS Admin. Bldg. Corvallis, OR 97331.]

——, D. B. Chelton, P. G. Strutton, and M. J. Behrenfeld, 2014: Satellite observations of chlorophyll, phytoplankton biomass, and Ekman pumping in nonlinear mesoscale eddies. *J. Geophys. Res. Oceans,* **118,** 6349–6370, doi:10.1002/2013JC009027.

Gill, A. E., 1982: *Atmosphere–Ocean Dynamics.* Academic Press, 662 pp.

——, J. S. Green, and A. J. Simmons, 1974: Energy partition in the large-scale ocean circulation and the production of mid-ocean eddies. *Deep-Sea Res.,* **21,** 497–528.

Henning, C. C., and G. K. Vallis, 2005: The effects of mesoscale eddies on the stratification and transport of an ocean with a circumpolar channel. *J. Phys. Oceanogr.,* **35,** 880–896.

Ibe, O. C., 2009: *Markov Process for Stochastic Modeling.* Elsevier, 490 pp.

Killworth, P. D., D. B. Chelton, and R. A. de Szoeke, 1997: The speed of observed and theoretical long extra-tropical planetary waves. *J. Phys. Oceanogr.,* **27,** 1946–1966.

Larichev, V. D., and I. M. Held, 1995: Eddy amplitudes and fluxes in a homogeneous model of fully developed baroclinic instability. *J. Phys. Oceanogr.,* **25,** 2285–2297.

Lawler, G., and V. Limic, 2010: *Random Walk: A Modern Introduction.* Cambridge University Press, 378 pp.

Maltrud, M. E., and J. L. McClean, 2005: An eddy-resolving global 1/10° ocean simulation. *Ocean Modell.,* **8,** 31–54.

Martin, A., and K. Richards, 2001: Mechanisms for vertical nutrient transport within a North Atlantic mesoscale eddy. *Deep-Sea Res. II,* **48,** 757–773.

McGillicuddy, D., and Coauthors, 2007: Eddy/wind interactions stimulate extraordinary mid-ocean plankton blooms. *Science,* **316,** 1021–1026.

——, J. Ledwell, and L. Anderson, 2008: Response to comments on ''Eddy/wind interactions stimulate extraordinary mid-ocean plankton blooms.'' *Science,* **320,** 448.

McWilliams, J. C., 1984: The emergence of isolated coherent vortices in turbulent flow. *J. Fluid Mech.,* **146,** 21–43.

——, and G. Flierl, 1979: On the evolution of isolated, nonlinear vortices. *J. Phys. Oceanogr.,* **9,** 1155–1182.

——, and Coauthors, 1983: The local dynamics of eddies in the western North Atlantic. *Eddies in Marine Science,* A. R. Robinson, Ed., Springer-Verlag, 92–113.

MODE Group, 1978: The mid-ocean dynamics experiment. *Deep-Sea Res.,* **25,** 859–910.

Müller, P., and C. Frankignoul, 1981: Direct atmospheric forcing of geostrophic eddies. *J. Phys. Oceanogr.,* **11,** 287–308.

Pedlosky, J., 1987: *Geophysical Fluid Dynamics.* Springer-Verlag, 710 pp.

Petersen, M. R., S. J. Williams, M. E. Maltrud, M. W. Hecht, and B. Hamann, 2013: A three-dimensional eddy census of a high-resolution global ocean simulation. *J. Geophys. Res. Oceans,* **118,** 1759–1774, doi:10.1002/jgrc.20155.

Priestley, M. B., 1987: *Spectral Analysis and Time Series.* Academic Press, 890 pp.

Rhines, P. B., 1975: Waves and turbulence on a beta-plane. *J. Fluid Mech.,* **69,** 417–443.

——, 1977: The dynamics of unsteady currents. *The Sea—Ideas and Observations on Progress in the Study of the Seas,* E. D. Goldberg, Ed., *Marine Modeling,* Vol. 6, John Wiley and Sons, 189–318.

——, 1979: Geostrophic turbulence. *Annu. Rev. Fluid Mech.,* **11,** 401–441.

Robinson, A. R., 1983: Overview and summary of eddy science. *Eddies in Marine Science,* A. R. Robinson, Ed., Springer-Verlag, 3–15.

——, and J. C. McWilliams, 1974: The baroclinic instability of the open ocean. *J. Phys. Oceanogr.,* **4,** 281–294.

Salmon, R., 1980: Baroclinic instability and geostrophic turbulence. *Geophys. Astrophys. Fluid Dyn.,* **10,** 25–52.

Samelson, R. M., 1990: Evidence for wind-driven current fluctuations in the eastern North Atlantic. *J. Geophys. Res.,* **95** (C7), 11 359–11 368; Corrigendum, 97 (C1), 821–822.

Schmitz, W. J., Jr., W. R. Holland, and J. F. Price, 1983: Mid-latitude mesoscale variability. *Rev. Geophys. Space Phys.,* **21,** 1109–1119.

Smith, K. S., 2007: The geography of linear baroclinic instability in Earth's oceans. *J. Mar. Res.,* **65,** 655–683.

——, and G. K. Vallis, 2002: The scales and equilibration of mid-ocean eddies: Forced–dissipative flow. *J. Phys. Oceanogr.,* **32,** 1699–1720.

Spall, M. A., 2000: Generation of strong mesoscale eddies by weak ocean gyres. *J. Mar. Res.,* **58,** 97–116.

Spitzer, F., 1976: *Principles of Random Walk.* Springer-Verlag, 395 pp.

Tulloch, R., J. Marshall, and K. S. Smith, 2009: Interpretation of the propagation of surface altimetric observations in terms of planetary waves and geostrophic turbulence. *J. Geophys. Res.,* **114,** C02005, doi:10.1029/2008JC005055.

——, ——, C. Hill, and K. S. Smith, 2011: Scales, growth rates, and spectral fluxes of baroclinic instability in the ocean. *J. Phys. Oceanogr.,* **41,** 1057–1076.

Venaille, A., G. K. Vallis, and K. S. Smith, 2011: Baroclinic turbulence in the ocean: Analysis with primitive equation and quasigeostrophic simulations. *J. Phys. Oceanogr.,* **41,** 1605–1623.

Weiss, J. B., 1999: Punctuated Hamiltonian models of structured turbulence. *Semi-Analytic Methods for the Navier–Stokes Equations,* K. Coughlin, Ed., CRM Proc. Lecture Notes, Vol. 20, Amer. Math. Soc., 109–119.

Wolfe, C. L., and P. Cessi, 2010: What sets the strength of the middepth stratification and overturning circulation in eddying ocean models? *J. Phys. Oceanogr.,* **40,** 1520–1538.

——, ——, J. L. McClean, and M. E. Maltrud, 2008: Vertical heat transport in eddying ocean models. *Geophys. Res. Lett.,* **35,** L23605, doi:10.1029/2008GL036138.

Wunsch, C., 1981: Low-frequency variability of the sea. *Evolution of Physical Oceanography,* B. A. Warren and C. Wunsch, Eds., MIT Press, 342–374.

——, 1999: Where do ocean eddy heat fluxes matter? *J. Geophys. Res.,* **104** (C6), 13 235–13 249.

Wyrtki, K., L. Magaard, and J. Hager, 1976: Eddy energy in the ocean. *J. Geophys. Res.,* **81** (15), 2641–2646.

Xu, Y., and L.-L. Fu, 2011: Global variability of the wavenumber spectrum of oceanic mesoscale turbulence. *J. Phys. Oceanogr.,* **41,** 802–809.